



Ultrathin MnO₂ nanosheets for optimized hydrogen evolution via formaldehyde reforming in water at room temperature

Lei Miao^a, Qing Nie^b, Jinlong Wang^{b,c,*}, Gaoke Zhang^c, Pengyi Zhang^d

^a School of Environmental Science and Engineering, Huazhong University of Science and Technology, Wuhan, 430074, China

^b School of Resources and Environmental Engineering, Wuhan University of Technology, Wuhan, 430070, China

^c Hubei Key Laboratory of Mineral Resources Processing and Environment, Wuhan University of Technology, Wuhan, 430070, China

^d State Key Joint Laboratory of Environment Simulation and Pollution Control, School of Environment, Tsinghua University, Beijing, 100084, China

ARTICLE INFO

Keywords:

MnO₂
Ultrathin structure
Oxygen vacancy
Formaldehyde
Hydrogen

ABSTRACT

Herein, we have developed a method for ultra-thinning MnO₂ nanosheets by H₂O swelling followed by a cetyltrimethylammonium bromide (CTAB)–intercalation exfoliation strategy. The thickness of the obtained U–MnO₂ nanosheets was about 1–2 layers. As-prepared U–MnO₂ exhibited higher turnover frequency (TOF) value of H₂ production from alkaline formaldehyde solution at room temperature as compared to that of pristine MnO₂ (TOF per surface Mn atom: 2.7 vs. 1.1 h^{−1}). With the ultra-thinning process, abundant surface oxygen vacancies (V_O) on U–MnO₂ were demonstrated by X-ray photoelectron spectroscopy and extended X-ray absorption fine structure analysis, which could couple molecular O₂ and benefit for the breaking of C–H bonds from formaldehyde with the generation of ·OOH radical. Detailed reaction–pathway calculations showed that the O₂ assisted dehydrogenation of alkaline HCHO solution were thermodynamically favored on U–MnO₂ with lower energy barrier of 0.32 eV as compared to that of 1.25 eV on pristine MnO₂. This work not only provides an applicable method for synthesizing ultrathin MnO₂ nanosheets but also gives an evidence towards more essential understanding of hydrogen evolution reaction from alkaline formaldehyde solution at atomic level.

1. Introduction

Hydrogen (H₂) has been regarded as a promising energy carrier by virtue of its high energy density and zero emission when burned with oxygen. [1,2], In recent decades, photocatalytic [3–6] and electrocatalytic [7–11] water splitting have been investigated and exhibited great prospect in the H₂ production; however, the low efficiency inhibited practical applications. In-situ H₂ release from a stable liquid by a methane or methanol–reforming process provides one of the ways ensuring its safe storage and high efficiency [12]. Recently, Ma et al. [13] reported the low-temperature (150–190 °C) H₂ production from methanol based on atomic Pt on α–MoC with an average turnover frequency (TOF) of 18,046 h^{−1} under neutral conditions. Formaldehyde (HCHO), as a widespread biomass fuel, is also used for H₂ evolution. Although the theoretical H₂ weight efficiency for H₂ production from HCHO (8.4 wt%) was slightly lower than that from methanol (12.5 wt %), most importantly, this reaction could be performed at room temperature, showing great prospect in utilizing low-cost organic reagents [14]. Moreover, considering the toxicity and environmental hazards of HCHO [15,16], it is a cleaner production process to directly utilize

formaldehyde for hydrogen generation instead of oxidizing it by traditional advanced oxidation methods.

Current research is mainly focused on precious metal catalysts for HCHO reforming process. Noble metals exhibit excellent performance due to their unique electrical, chemical, optical, and catalytic properties [17]. Bi et al. found that Pd-based materials, including pure Pd nanorods [18] or Pd/TiO₂ [19] catalysts, could achieve an efficient H₂ production from alkaline HCHO solution. Li et al. [20] found that Ag/MgO could achieve an H₂ production with a TOF value up to 6600 h^{−1} under neutral conditions. MgO-based Au, Cu, Ru, and Rh also exhibited good H₂ evolution activities [21]. Moreover, homogeneous catalysts, such as Ru-based catalysts [14], could also exhibit an excellent H₂ evolution efficiency without requiring alkaline conditions. In order to achieve a high H₂ production rate of the reaction between HCHO and H₂O at low temperatures, both the dehydrogenation process from HCHO or H₂O must be activated effectively during the whole H₂ evolution process. It was found that the ·OOH radical is a key free radical species in the HCHO dehydrogenation process, which was derived from a 2-electron oxygen reduction reaction in the presence of HCHO [20]. Traditional transition metal oxides, such as MnO₂, with certain defects

* Corresponding author.

E-mail address: wjl16@whut.edu.cn (J. Wang).

<https://doi.org/10.1016/j.apcatb.2019.02.047>

Received 20 October 2018; Received in revised form 10 February 2019; Accepted 17 February 2019

Available online 19 February 2019

0926-3373/© 2019 Elsevier B.V. All rights reserved.

on the surface, can act as active site and couple O_2 to generate active $\cdot O_2^-$ species (precursor of $\cdot OOH$ radical) [22]. MnO_2 polymorphs with abundant Mn^{3+} species were regarded as an intriguing type of catalysts for the H_2O oxidation reaction [23]. In addition, layered MnO_2 exhibits hydrophilic property and can adsorb H_2O molecules on its surface in various ways, including physically adsorbed H_2O , structural interlayer H_2O , and surface hydroxyl groups, achieving good ability for H_2O adsorption and dissociation [24]. Considering the excellent properties of the two aspects of layered MnO_2 , it is possible for its H_2 evolution reaction.

Two-dimensional (2D) materials have produced a wide range of applications due to their unique geometric and electronic structure [25,26]. In the field of catalysis, by decreasing the thickness to atomic dimensions, surface atoms can easily escape from the lattice to form vacancy defects, which further decreases the coordination number of the neighboring atoms and increases the number of reactive sites [27]. In addition, the ultrathin structure strongly affects the electronic structure, which in turn plays an important role in tuning the activity of the reactive sites and hence affects their catalytic properties [28]. Strong interactions could be observed at contacted interface on $AuNP@MnO_2$ ultrathin nanosheet with the generation of partially oxidized Au^+ , benefiting for electrocatalytic oxygen reduction reactions [29]. Thus, by applying the ultra-thinning process to layered MnO_2 , its catalytic properties may be greatly enhanced. The conventional method for preparing ultrathin MnO_2 nanosheets is the tetrabutylammonium or tetramethylammonium hydroxide (TBAOH or TMAOH) intercalation method, which takes a long time and requires acid treatment to replace previous interlayer cations by protons in advance [30,31]. It has been reported that redistributed 4f electrons of Mn^{3+} ions could feedback to the $\pi 2py^*$ orbital of O to couple O_2 and generate $\cdot O_2^-$ species [32,33]. However, the disproportionation of Mn^{3+} ions occurring during acid soaking could decrease the content of Mn^{3+} [34], which would be harmful to the activation of O_2 . Thus, there is a need to develop a new method for synthesizing ultrathin MnO_2 nanosheets.

Herein, we have developed a method for ultra-thinning MnO_2 nanosheets by H_2O swelling followed by a cetyltrimethylammonium bromide (CTAB)-intercalation exfoliation strategy. The thickness of the obtained ultrathin MnO_2 nanosheets (U- MnO_2) was about 1–2 layers. With the ultra-thinning process, more oxygen vacancies (V_O) were generated on U- MnO_2 , leading to strong coupling between the catalyst surface and molecular O_2 , which was beneficial for the subsequent dehydrogenation process. As a result, the as-prepared U- MnO_2 exhibited higher turnover frequency (TOF) value of H_2 production as compared to the pristine MnO_2 (2.7 vs. $1.1 h^{-1}$). Combined with experimental and theoretical investigations, we presented the key active sites and H_2 evolution mechanism. This is the first work that using metal oxides in H_2 evolution reaction from HCHO solution. Significances of defects effect in the H_2 evolution reaction were clarified, providing guidance in directly designing active metal oxide catalysts or developing useful noble metal-supported carriers.

2. Experimental section

2.1. Materials synthesis

Synthesis of pristine MnO_2 nanosheets. MnO_2 nanosheets were prepared by a simple method reported in the literature [35]. In detail, 1.0 g $KMnO_4$ and 0.15 g $MnSO_4 \cdot H_2O$ were dissolved in 70 mL deionized water. After that, the solution was transferred to a hydrothermal reactor. The temperature was kept at $200^\circ C$ for 12 h. The final precipitate was centrifuged and washed three times to remove possible residual impurities. Then, the precipitate was dried in an oven at $105^\circ C$ for 12 h. Finally, the sample was calcined in a muffle furnace at $300^\circ C$ for 3 h.

Exfoliation of pristine MnO_2 to ultrathin nanosheet structure. U- MnO_2 nanosheets were obtained via H_2O -swelling followed by the CTAB-intercalation strategy. In detail, 0.4 g MnO_2 and 0.575 g CTAB

were dissolved in 70 mL of deionized water. After thorough stirring, the mixed solution was transferred to a hydrothermal reactor and maintained at $150^\circ C$ for 12 h. The dark brown suspension was first centrifuged at 500 rpm for 10 min to remove the non-exfoliated component, then centrifuged at 8000 rpm, and finally washed with deionized water. Then, the precipitate was dried in an oven at $105^\circ C$ for 12 h.

2.2. Characterizations

Transmission electron microscopy (TEM) and atomic force microscopy (AFM) were carried out for morphology analysis. X-ray diffraction (XRD) patterns, Raman shift spectra, nitrogen adsorption-desorption experiments, X-ray photoelectron spectroscopy (XPS), hydrogen temperature-programmed reduction (H_2 -TPR), oxygen temperature-programmed desorption (O_2 -TPD), and extended X-ray absorption fine structure (EXAFS) patterns were used to characterize the physical and chemical properties. Electron spin response (ESR) was carried out for the detection of generated free radicals. Theoretical calculations were performed with the CASTEP package for surface adsorption energy calculation, density of state analysis, and transition state calculation. More details were presented in Supplementary Information.

2.3. H_2 evolution experiments

H_2 evolution from alkaline HCHO solution was studied in a sealed quartz reactor (450 mL) by adding 95 mL alkaline HCHO solution (Figure S1). A water bath was used to maintain the reaction temperature. The O_2 pressure (0, 0.04, 0.21, and 0.99 atm.) in the reactor was adjusted by purging with pure O_2 gas for a certain time. In addition, the concentrations of NaOH (0, 0.1, 0.5, 1.0, and 1.5 M) and HCHO (0, 0.5, 1.5, and 2.0 M) were also varied. Then, 20 mg of the samples was ultrasonically dispersed in 5 mL of deionized water and subsequently injected into a glass reactor via a syringe to trigger the catalytic H_2 evolution reaction. At regular time intervals (10 min), gas volumes of 200 μL were withdrawn from the glass reactor at the seal using a micro-liter syringe, and the amounts of evolved gases, including H_2 , O_2 , and CO, were analyzed by gas chromatography on a GC-2014 instrument (Shimadzu, Japan) equipped with a thermal conductivity detector. Argon gas was used as carrier gas. To calculate the apparent activation energy (E_a), H_2 evolution experiments were performed at different temperatures ranging from 10 to $25^\circ C$. For TOF calculation, the crystal lattice parameter and corresponding specific surface area of layered MnO_2 were used to quantify the amount of surface exposed Mn atoms. In details, the unit cell of layered MnO_2 exhibited length $5.149 \times 7.176 \text{ \AA}$ with 2 Mn atoms on a face, the density of surface Mn atoms was estimated to be $5.5 \times 10^{18} \text{ atoms/m}^2$. By using BET surface area, we could obtain the content of surface exposed Mn atom. The related formula is listed below:

$$TOF (h^{-1}) = \frac{n_{H_2} \times N_A}{S_{BET} \times M \times D} \times 10^{-3}$$

Where n_{H_2} is the generated H_2 (μmol) within 1 h, N_A is Avogadro constant (atoms/mol), S_{BET} the specific surface area (m^2/g), M is sample weight (mg), D is the density of surface Mn atoms ($atoms/m^2$).

3. Results and discussion

3.1. Catalyst synthesized process and corresponding characterizations

Ultrathin MnO_2 nanosheets were synthesized by water swelling followed by CTAB-intercalation exfoliation, as illustrated in Fig. 1a. Layered MnO_2 is composed of edge-sharing $[MnO_6]$ octahedra containing a certain number of water molecules and cations (K^+ , as illustrated) between the layers [35]. Here, the high temperature of $150^\circ C$ increased the thermal motion of the water molecules between the layers, weakening the van der Waals force between the layers. As a

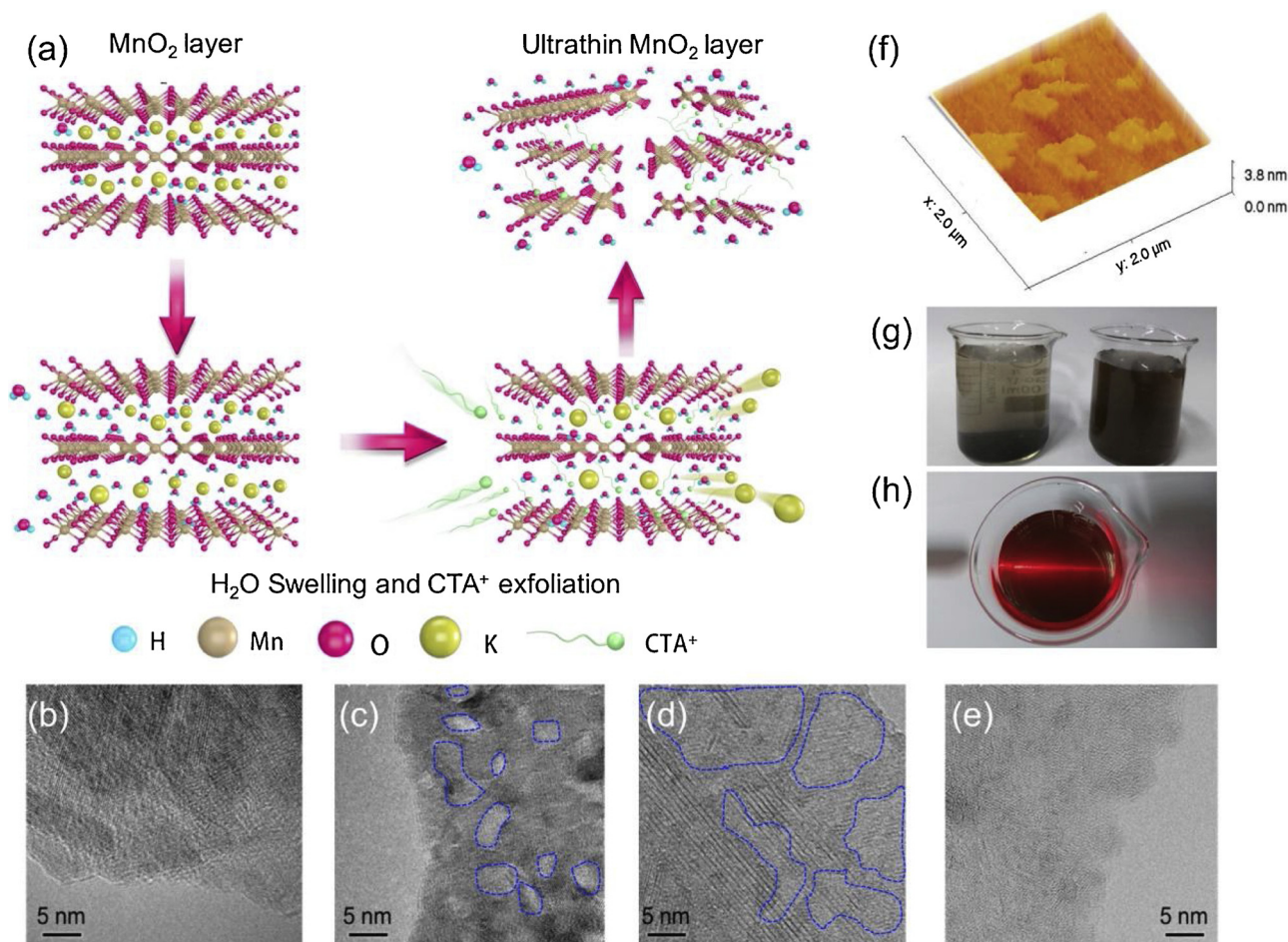


Fig. 1. (a) Schematic illustration for H₂O swelling and CTA⁺ exfoliation process from bulk MnO₂ to ultrathin MnO₂ nanosheets. (b)–(e) Surface morphology changes with different stages of exfoliation time (0, 1, 6, 12 h). (g) AFM image of the as-obtained nanosheets. (g) Photos of MnO₂ and U-MnO₂ suspensions. (h) Laser scattering of U-MnO₂.

result, more water molecules can enter and swell the layers to expand the interlayer spacing. At the same time, the surfactant cations of CTA⁺ gradually penetrate into the interlayers along the fissure and exchange with the K⁺ ions between the layers, triggering the expansion and subsequent exfoliation of layered MnO₂ due to its spatial size effect. TEM images of the morphological changes at different stages of exfoliation time are illustrated in Fig. 1b–e. Pristine MnO₂ nanosheets exhibited relatively smooth surfaces, and the dark contrast indicates that they are composed of several stacked layers (Fig. 1b). During the whole exfoliation process, irregular pits with a diameter of about 5 nm could be first observed (Fig. 1c), which was similar to our previous work. The space steric effect of CTA⁺ could weaken the van der Waals force between the interlayers, and the layers were burst with numerous irregular pores on their surface. When the reaction time was extended to 6 h, larger areas of the surface layer were peeled off. It can be concluded that the introduction of CTAB facilitated peeling of the surface layers from outside to inside layers. Finally, further prolonging the reaction time to 12 h resulted in the formation of ultrathin MnO₂ nanosheets, as indicated by the light contrast of their morphology visualized in TEM. Three-dimensional (3D) AFM images (Fig. 1f) showed that, after exfoliation, the ultrathin MnO₂ nanosheets consisted of irregular fragments with lateral sizes of 200 nm or more. Furthermore, the suspensions of pristine MnO₂ and U-MnO₂ dissolved in water are shown in Fig. 1g. Pristine MnO₂ easily precipitated in water, while U-MnO₂ nanosheets exhibited a uniform dispersion state in the solution due to the ultrathin layered structure. The Tyndall light-scattering phenomenon was also observed, confirming that the U-MnO₂

nanosheet suspension was highly dispersed (Fig. 1h).

TEM and HRTEM images of pristine MnO₂ and U-MnO₂ are illustrated in Fig. 2. Both samples exhibited interleaving nanosheet structures. U-MnO₂ showed a light contrast as compared to pristine MnO₂ due to its ultrathin and transparent lamellar structure. Pristine MnO₂ (Fig. 2b, c) exhibited a fringe spacing of 0.71 nm, which matches well with the theoretical value of the [001] planes of layered MnO₂, indicating that mainly the ab-plane of the ultrathin MnO₂ nanosheets was exposed [36]. Viewing along the [001] facet, six or seven layers could be distinguished, indicating that the thickness of pristine MnO₂ was about 5 nm. In the direction perpendicular to the [001] crystal facet, fringe spacing of 0.24 nm was observed, corresponding to the [100] crystal plane of layered MnO₂. The presence of a weak reflection ring of the electron diffraction in the selected area indicates that MnO₂ possesses a polycrystalline structure. As for U-MnO₂ (Fig. 2e, f), the layered slab exhibited a disordered structure in c-axis, indicating the chemical interaction between the layers was weakened. In addition, the grid spacing in U-MnO₂ seems to be more irregular than that of pristine MnO₂, suggesting that more defective sites appeared on the surface of the (001) crystal facet during the exfoliation process. Correspondingly, the thickness of the MnO₂ nanosheets was also detected by tapping-mode AFM (Fig. 3). The height profile scan of the pristine MnO₂ nanosheets along the red line showed a fairly flat nanosheet surface with an approximate thickness of 3.4 or 4.8 nm, corresponding to a total stack of 5 or 7 layers (the thickness of a single-layer MnO₂ slab along the [001] direction is about 0.71 nm). As for U-MnO₂, the thickness of the nanosheets measured by AFM is about 0.8–1.1 nm (the hydrated

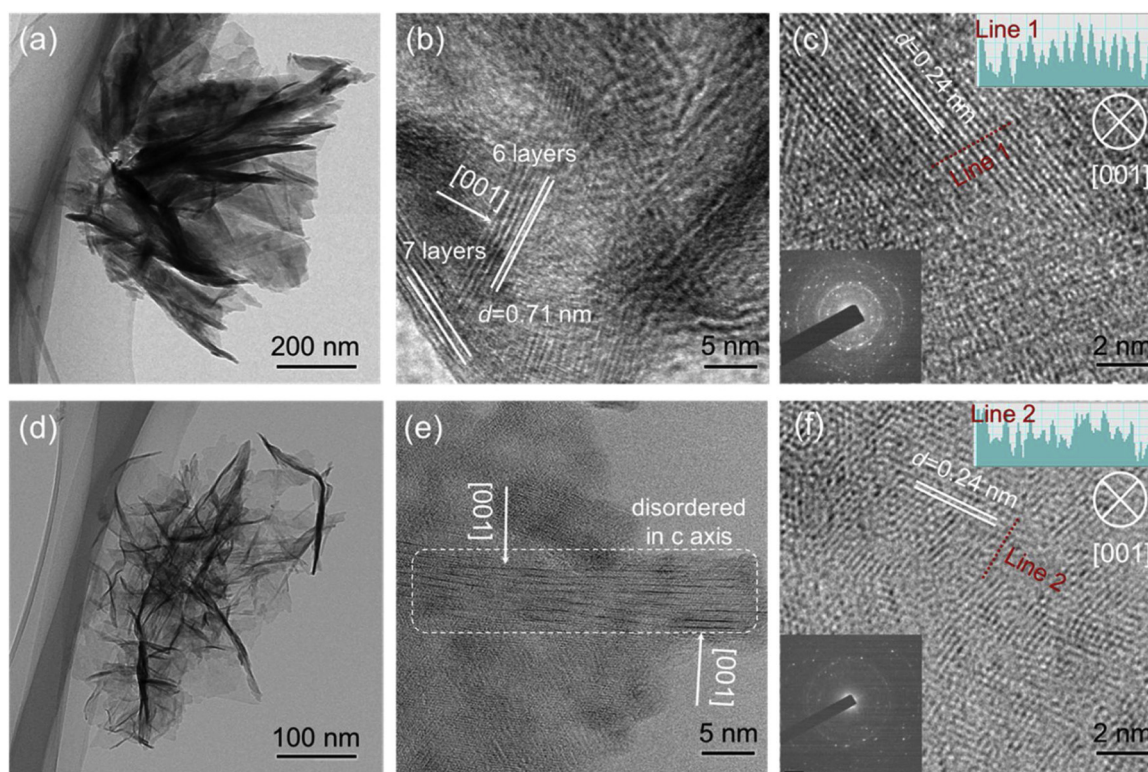


Fig. 2. TEM and HRTEM images of (a–c) MnO_2 , and (d–f) U-MnO_2 . The electron diffraction patterns and line profiles showing the image intensity of the position along Line1 and Line 2 were both illustrated in insert figure of (c) and (f).

MnO_2 slab is a little thicker than the theoretical value of 0.30 nm [31]). This finding is in good agreement with the unit cell of layered MnO_2 along the c -axis, suggesting that U-MnO_2 mostly consists of one or two atomic layers.

The crystalline structure of exfoliated U-MnO_2 was characterized by XRD analysis. As shown in Fig. 4a, peaks located at 12.4° , 24.6° , 36.5° , and 65.5° agreed well with the (001), (002), (100), and (110) planes of the monoclinic structure of MnO_2 (C12/m1) with lattice constants of $a = 5.149 \text{ \AA}$, $b = 2.842 \text{ \AA}$, and $c = 7.047 \text{ \AA}$ [37]. The diffraction peak at 12.4° , which is sharp in comparison with those of other planes, indicated that the (001) plane was dominating and exhibited a relatively long-ranged order. However, as for exfoliated U-MnO_2 , the intensity of the (001) peak significantly decreased, and the 2-theta position slightly downshifted from 12.4 to 12.2° , corresponding to an increase in the interplanar distance from 7.1 to 7.2 \AA . This result indicates an extended stacking in c -direction during the formation of ultrathin MnO_2 nanosheets. The grain size of different samples based on the width and position of the diffraction peak of MnO_2 at the (001) plane (inset of Fig. 4a) was also calculated. The results indicated that the grain size of U-MnO_2 was smaller compared with pristine MnO_2 (10.4 nm vs. 15.7 nm), indicating more Mn atoms are exposed on the surface, i.e., U-MnO_2 sample owned higher Mn dispersion. More details were shown in Supplementary Information. Raman spectroscopy is useful for analyzing the local structure of materials, especially those with the same crystal lattice but different lattice orders. Raman shift positions located at 640 and 575 cm^{-1} were assigned to the symmetric stretching vibration of the Mn–O bond in the $[\text{MnO}_6]$ groups vertical or parallel to the basal (001) plane (Fig. 4b) [38]. Compared with pristine MnO_2 , the Mn–O stretching vibration vertical to the basal (001) plane in exfoliated U-MnO_2 shifted by 5 cm^{-1} to lower wavenumbers, indicating that a weak interlayer interaction occurred due to a more relaxed confinement effect in vertical direction. In addition, the Mn–O stretching vibration of the basal plane in exfoliated U-MnO_2 almost disappeared compared with pristine MnO_2 . This can be explained by lattice distortion during

the exfoliation process, which breaks the crystal symmetry and lowers the spectroscopic symmetry. Peeling off the layer inevitably could result in leaking of more surface atoms, increasing the specific surface area [39]. Herein, Brunauer–Emmett–Teller (BET) analyses of N_2 adsorption and desorption (type IV) were carried out to evaluate the specific surface areas of the different samples (Fig. 4c). U-MnO_2 exhibited a specific surface area of $234.1 \text{ m}^2/\text{g}$, which is much higher than that of pristine MnO_2 ($101.3 \text{ m}^2/\text{g}$), indicating that the here developed method of H_2O swelling and CTAB ion intercalation is highly efficient for generating single- or few-layered MnO_2 nanosheets. The process of ultra-thinning 2D materials could change the local atomic environment, altering the surface chemical state. XPS K 2p spectra displayed in Fig. 4d show that the intensity of the XPS K2p peak of U-MnO_2 is lower than that of pristine MnO_2 , indicating that ion exchange occurred between CTAB and interlayer K^+ ions. In addition, the binding energy of the XPS K 2p peak in U-MnO_2 shifted to a lower value (290.4 eV) with respect to that of pristine MnO_2 (291.3 eV). In pristine MnO_2 , the K^+ ions are confined between the interlayers and balance the Mn^{3+} charge. The K 2p and adjacent O 2p orbitals are hybridized, which reduces the charge density of the K^+ ions [40]. However, when the MnO_2 nanosheets peeled off, the chemical interactions between the K^+ ions and the layers weakened, and the K^+ ions existed in a kind of isolated state of high charge density, [34,41]. The increase of charge density of the K^+ ions in U-MnO_2 further demonstrated that the MnO_2 nanosheets were successfully stripped into an ultrathin structure. In addition, the Mn 2p and O 1s spectra of pristine MnO_2 and U-MnO_2 (Figure S2) showed that the molar $\text{Mn}^{3+}/\text{Mn}^{4+}$ ratio of U-MnO_2 (2.58) is much higher than that of pristine MnO_2 (1.14), which can be explained by the possible existence of surface vacancies (charge decrease of Mn^{4+} due to the depletion of surface oxygen [42]) resulting from the exfoliation process. Consistently, U-MnO_2 exhibited a higher content of surface-adsorbed oxygen (O_{ads}), which is possibly related to the consequent generation of V_O during the exfoliation process where O_2 or H_2O from the gas phase can adsorb dissociatively on such defects [22,32]. To

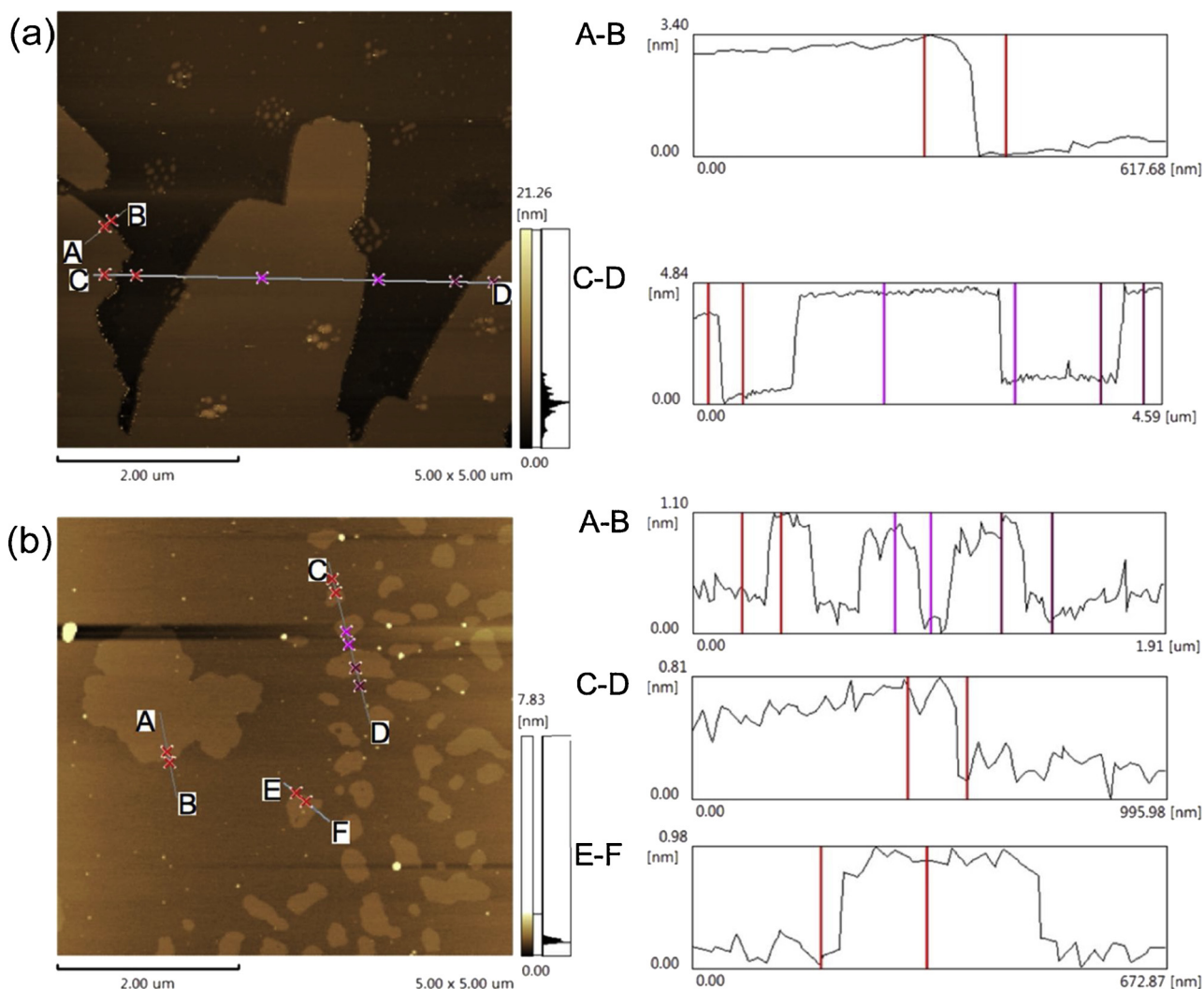


Fig. 3. AFM images and the corresponding height profiles of (a) MnO_2 , and (b) U-MnO_2 .

demonstrate the surface defects information at atom level, EXAFS was carried out to simulate the surface coordination structure. The different local atomic arrangements around Mn atom in MnO_2 and U-MnO_2 were displayed in the corresponding R -space (Fig. 5a) and k -space spectra (Fig. 5b). The Mn EXAFS spectra exhibited two main peaks in R -space spectra corresponding to the Mn–O and Mn–Mn shells, respectively [43]. The $\beta\text{-MnO}_2$ (Mn–O length is 1.93 Å; Coordination number (CN) is 6) and Mn_2O_3 (Mn–Mn length is 2.89 Å; CN is 6) were selected as reference samples for the simulation according to our previous research [44]. As shown in Table S1, the Mn–O length was calculated to be 1.89 Å in U-MnO_2 , which was shorter than that of pristine MnO_2 (1.90 Å), indicating the possible deficiency of surface oxygen atom in U-MnO_2 sample [45]. Similarly, the decreased CN of Mn–O in U-MnO_2 was also observed (5.4 vs. 5.9) compared with pristine MnO_2 sample, further indicating more V_O were generated when the MnO_2 sheet thickness was reduced to 1 or 2 atomic layers. Zhao et al. [46] also reported the existed V_O on ultrathin $\delta\text{-MnO}_2$ nanosheet. Additionally, the bond length (R) and CN of Mn–Mn were also calculated (Table S1). Although the coexistence of Mn vacancy and V_O in monolayered MnO_2 has been reported by Xie's group, [37] the coordination environment of Mn–Mn atoms did not vary too much, indicating the structural distortion in U-MnO_2 was mainly caused by V_O . In addition, the electron density of states (DOS) of pristine MnO_2 and U-MnO_2 were also calculated (Fig. 5c and d). The valence and conduction bands of MnO_2 mainly corresponded to the hybrid of Mn 3d and O 2p orbitals. Pristine MnO_2

exhibited charge localization at the Fermi level, exhibiting a wide band gap. With respect to U-MnO_2 (one oxygen was removed from the MnO_2 slab in the calculated model), a new intermediate band state occurred due to the presence of V_O , effectively narrowing the band gap and thus rendering enhanced electrical conductivity and electron mobility. The band gaps of U-MnO_2 and pristine MnO_2 were measured according to Tauc plot transformed from diffuse reflectance spectra. As shown in Figure S3, energy gap of MnO_2 and U-MnO_2 were calculated to be 2.2, and 2.0 eV, respectively. It was palpable that U-MnO_2 has a smaller energy gap than pristine MnO_2 , which was consistent with the results simulated by DFT calculation. Sun et al. [47] also reported that the presence of V_O in ultrathin CeO_2 could facilitate fast CO diffusion along the two-dimensional conducting channels. Thus, with the ultra-thinning process, more V_O were generated on U-MnO_2 , leading to strong coupling between the catalyst surface and molecular O_2 , which was beneficial for the subsequent dehydrogenation process.

To further investigate the reducibility of the samples and discriminate the roles of O_2 , H_2 -TPR and O_2 -TPD were carried out accordingly. The results of H_2 -TPR are displayed in Figure S4a. With the increase of reduction temperature, the sample will undergo the reduction of surface adsorbed oxygen species, and the process of $\text{MnO}_2 \rightarrow \text{Mn}_2\text{O}_3 \rightarrow \text{Mn}_3\text{O}_4 \rightarrow \text{MnO}$. The reduction peak in U-MnO_2 was located at 245 and 269 °C, both lower than that of pristine MnO_2 sample, indicating the lattice oxygen could be more easily reduced on U-MnO_2 . During the ultra-thinning process of the two-dimensional materials,

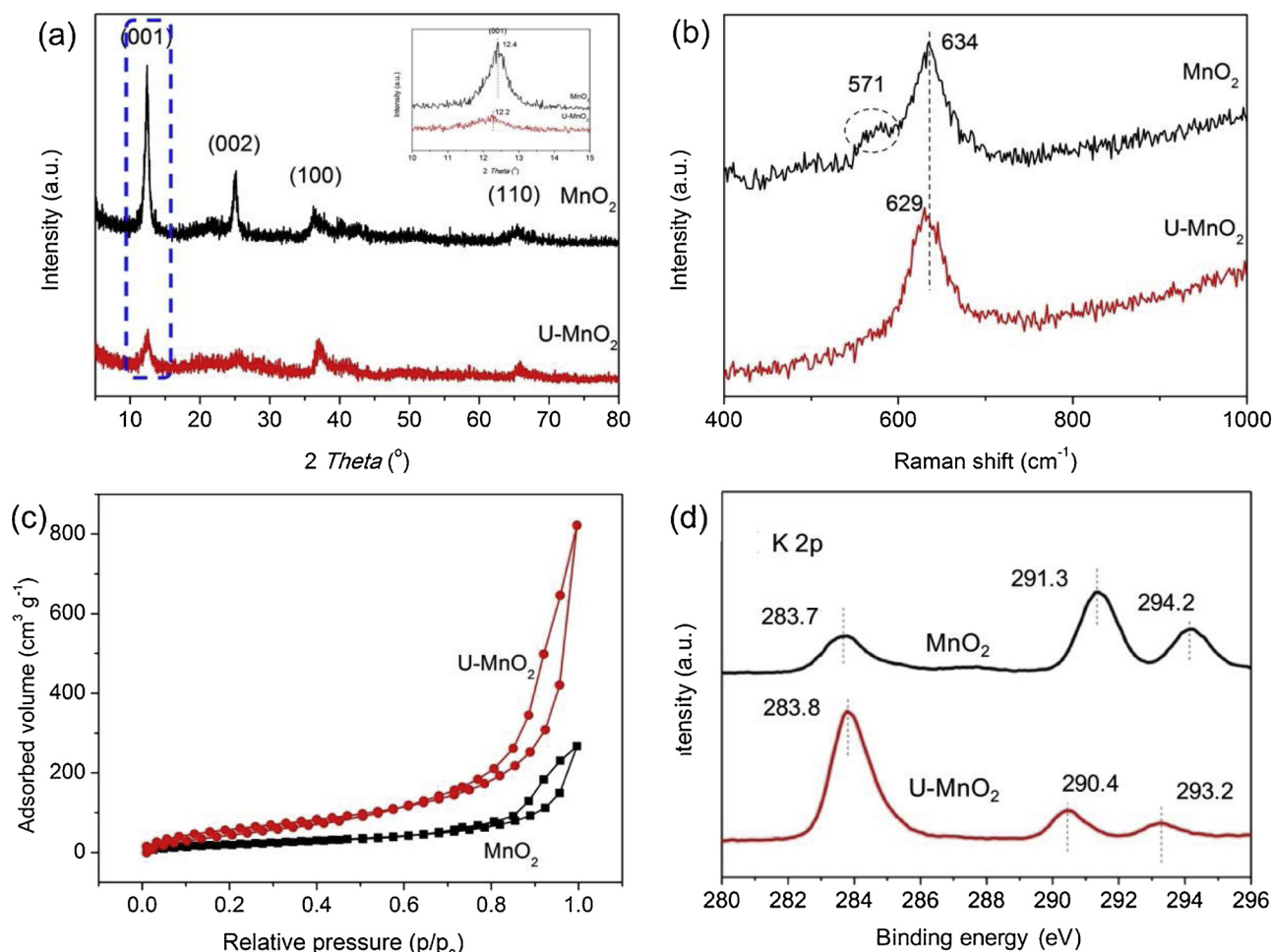


Fig. 4. Structure characterizations of MnO₂ and U-MnO₂: (a) XRD patterns, (b) Raman shift spectra, (c) N₂-desorption and sorption isotherm, and (d) K 2p XPS spectra.

the surface atoms could be easily escaped from (001) crystal plane due to the disappearance of interlayer confinement along the *c*-axis direction, which could result in the mobility of lattice oxygen. In addition, the onset reduction temperature of U-MnO₂ was a little lower than that of pristine MnO₂ (the inset of Figure S4a). The easy reduction of U-MnO₂ may be derived from the easy formation of surface adsorbed oxygen such as superoxide radicals ($\cdot\text{O}_2$) at V_O site. Furthermore, the O₂-TPD was also carried out to characterize the O₂ adsorption abilities over different samples (Figure S4b). With the increase of desorption temperature, different types of oxygen will be released followed by surface adsorbed, surface lattice oxygen, and bulk lattice oxygen, respectively [34]. As for U-MnO₂, the onset reduction temperature started before 118 °C, which was much lower than that of pristine MnO₂ sample, indicating surface adsorbed oxygen were easily formed on U-MnO₂ sample. Since oxygen molecules are usually adsorbed at the oxygen vacancies of an oxide material, it is reasonable to deduce that U-MnO₂ owned the largest amount of oxygen vacancies and exhibited strong oxygen adsorption and activation capacity.

3.2. H₂ evolution performance

The H₂ evolution efficiencies of pristine MnO₂ and U-MnO₂ were tested in alkaline HCHO solution at room temperature. As shown in Fig. 6a, in a blank environment (1.5 M HCHO, 1 M NaOH, temperature of 30 °C, 0.22 atm. of O₂), almost no H₂ was generated. After the addition of MnO₂, constant evolution of H₂ gas was immediately observed without any induction period, and no detrimental CO was detected

during the entire reaction period (Figure S5). The H₂ production after 60 min was about 20.4 μmol, corresponding to a turnover frequency (TOF) value per surface Mn atom of 1.1 h⁻¹. U-MnO₂ exhibited a better H₂ evolution efficiency, as 112.7 μmol H₂ have been generated after 60 min, corresponding to a TOF value of 2.7 h⁻¹. The result indicated the unique ultrathin structure was beneficial for the H₂ evolution reaction. The apparent activation energy (E_a) was also calculated from Arrhenius plots for the different samples at different reaction temperatures (10, 15, 20, and 25 °C, respectively; Figures S6a and 6b). The E_a values of MnO₂ and U-MnO₂ were 36.4 and 26.1 kJ/mol, respectively, indicating that H₂ is more easily generated on U-MnO₂ than on pristine MnO₂. High temperature can facilitate the H₂ evolution reaction. However, too high temperature will definitely inhibit the reaction. As shown in Fig. 6a and Figure S6, sample exhibited higher reaction rate at the initial reaction stage, however, reaction rate decreased with the prolonged of reaction time. More obvious declines could be observed at higher temperature. As we all know, MnO₂ is also a kind of oxidant, which can directly oxidize formaldehyde into formic acid or CO₂. When the reaction temperature is too high, the $\cdot\text{H}$ radicals derived from HCHO or H₂O molecular might be quenched into H₂O by oxidant instead of forming H₂.

Factors influencing the H₂ evolution (e.g., alkaline concentration, HCHO concentration, and partial O₂ pressure) are demonstrated. In detail, base additives are commonly used in HCHO reforming reactions. In Figure S7a, no obvious H₂ evolution was detected without the addition of NaOH, suggesting that alkaline conditions are crucial for this catalytic process. As the NaOH concentration increased from 0.25 to

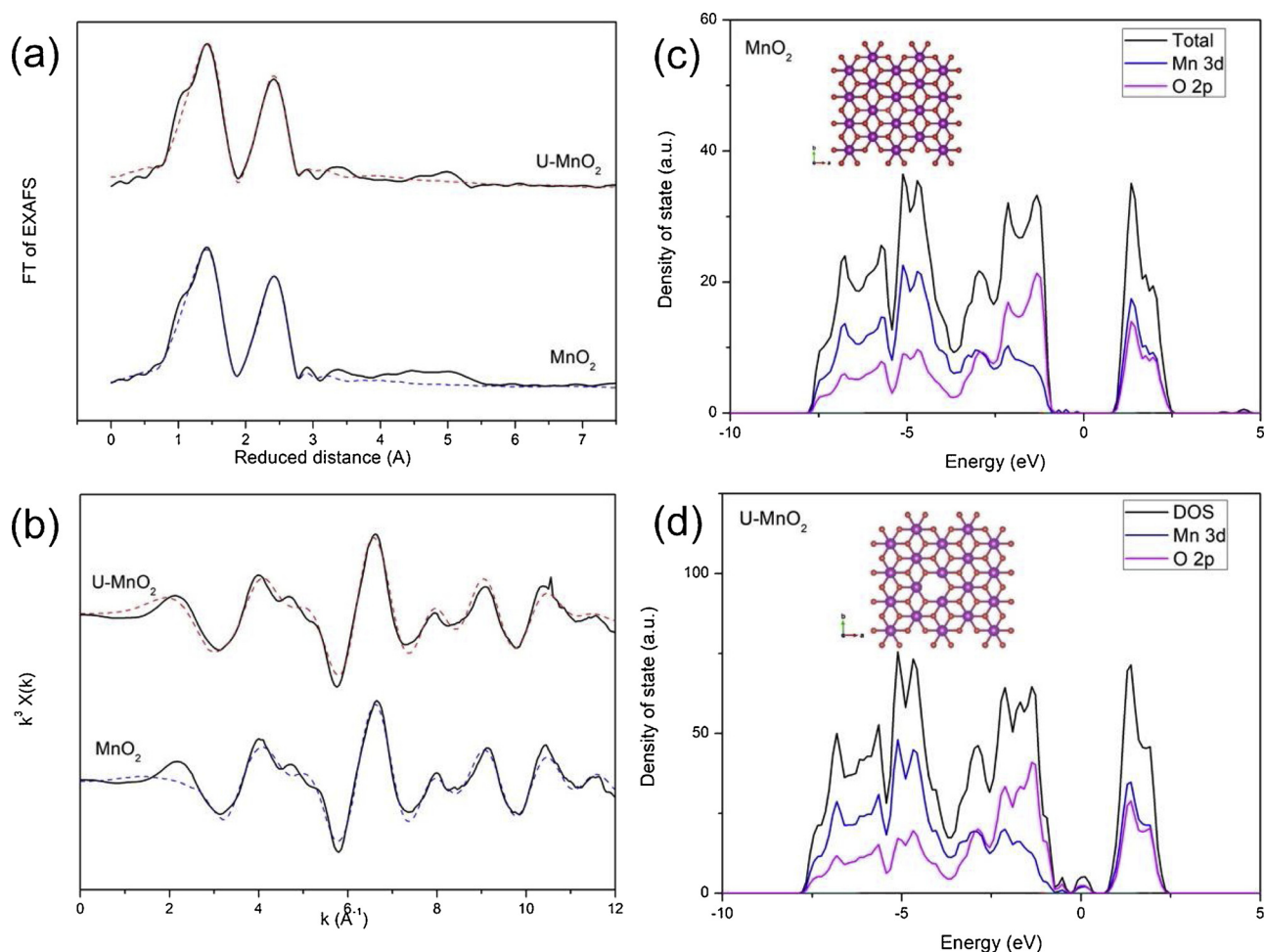


Fig. 5. (a) Fourier-transformed Mn K-edge EXAFS oscillation function spectra, (b) magnitude of k^3 -weighted spectra. Dashed lines are fitted curve. (c), (d) Density of state over different samples. Insert figures are the top view structure of MnO_2 with and without O vacancy presenting MnO_2 and U-MnO_2 samples. O in red, Mn in dark purple, and K^+ and H_2O are all relaxed (For interpretation of the references to colour in this figure legend, the reader is referred to the web version of this article).

1.0 M, the H_2 evolution in 60 min increased from 34.1 to 55.6 μmol . However, when the NaOH concentration further increased to 1.5 M, the H_2 evolution decreased to 35.7 μmol . Too high NaOH content would inhibit the H_2 evolution reaction in favor of the competing Cannizzaro reaction for transforming formaldehyde into methanol and formic acid

under highly alkaline conditions. In addition, the HCHO concentration played a crucial role in determining the H_2 production rate. The highest H_2 production rate was obtained for 1.5 M HCHO (Figure S7b). These results showed that the concentration of HCHO and NaOH should be controlled properly in order to achieve high H_2 production rates. Li

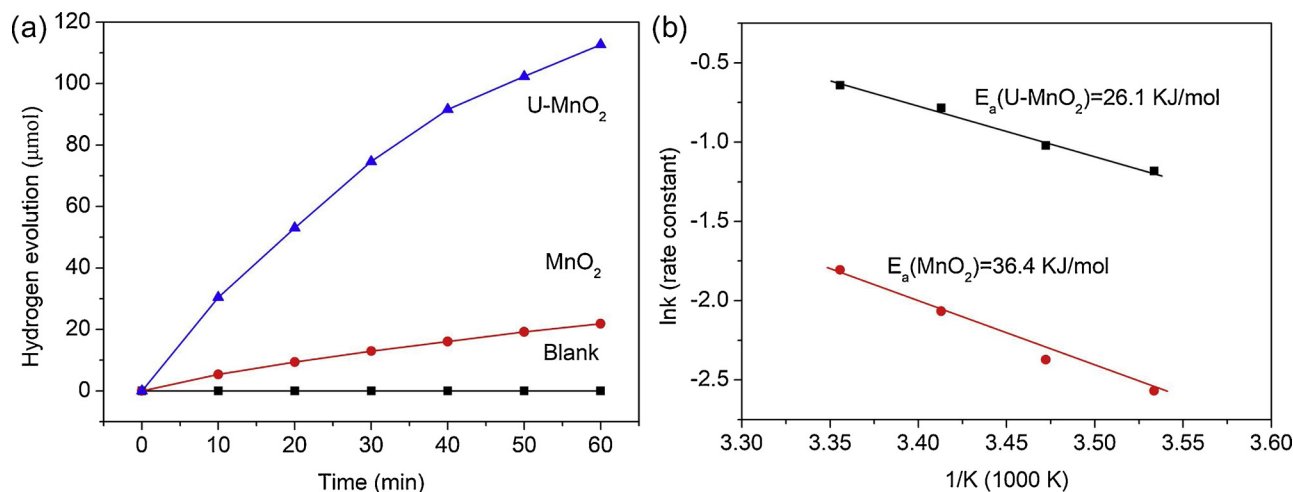


Fig. 6. (a) hydrogen production over MnO_2 and U-MnO_2 samples. NaOH: 1 mol/L, HCHO: 1.5 mol/L, catalyst: 20 mg, reaction temperature: 30 °C. (b) The calculation of activation energy for MnO_2 and U-MnO_2 samples.

et al. [20] reported that molecular O_2 can act like a catalyst in Ag/MgO catalysts, promoting the generation of $\cdot OOH$ radicals in the reaction system. The generation of $\cdot OOH$ radicals contributed to the dehydrogenation of HCHO molecules. Here, a similar phenomenon was for the U- MnO_2 catalyst (Figure S7c). The H_2 evolution increased from 20.7 to 231.6 μmol with the increase of the O_2 partial pressure from 0.045 to 0.99 atm., indicating that O_2 is exerting a promoting effect. More discussion about these influencing factors will be presented in the mechanism part.

The cycling experiment for H_2 production by U- MnO_2 was preformed to evaluate its stability. After each test, samples were centrifuged and dried in an oven for the use of next batch. As illustrated in Figure S8, no obvious declines could be observed. After five cycles, the H_2 production in 60 min by U- MnO_2 decreased slightly from 115.6 to 95.4 μmol , mainly resulted from the mass loss of samples in the recycling processes. Moreover, the structure of U- MnO_2 used before and after HCHO reforming reaction were also compared (Figure S9). No obvious changes could be observed on its XRD patterns, further indicating the stability of U- MnO_2 sample.

3.3. Mechanism

To confirm the formation of active free radical species during the H_2 evolution process, ESR spin-trapping experiments were carried out. Four key free radical species form during the H_2 evolution reaction in the HCHO solution. The splitting mode and the corresponding shape of DMPO-trapped free radicals, including $\cdot H$ radicals ($A_N = 16.5$ G, $A_{H1} = A_{H2} = 22.5$ G), $\cdot OH$ radicals ($A_N = A_H = 16.4$ G), $\cdot OOH$ radicals

($A_N = 14.8$ G, $A_{H1} = 13.7$ G, $A_{H2} = 1.5$ G), and $\cdot CO$ radicals ($A_N = 15.7$ G, $A_H = 8.4$ G) are shown in Fig. 7a. As a commonly used water oxidation catalyst, $\cdot H$ and $\cdot OH$ radicals result mainly from the dissociation of chemisorbed H_2O on the MnO_2 surface [32]. Traces of $\cdot H$ and $\cdot OH$ radicals were observed for MnO_2 in aqueous environment, further demonstrating the source of these radicals (Figure S10a and S10b). The $\cdot OOH$ radicals are mainly formed together with the remaining $\cdot CO$ radicals by the combination of superoxide and hydrogen radicals that were removed by C–H bond cleavage of molecular HCHO, regarding as the key active species during the H_2 evolution reaction from HCHO. In the blank aerobic experiment of the suspension containing alkaline HCHO solution and DMPO without the addition of the MnO_2 catalyst, almost no characteristic free radicals were observed, indicating a very slow hydrogen evolution reaction rate at room temperature (Figure S10c). In Figure 7b, when pristine MnO_2 was added to the suspension, $\cdot OH$ radicals were detected immediately; their amount increased with the reaction time, and they dominated during the whole reaction. However, only a small portion of $\cdot H$, $\cdot OOH$, and $\cdot CO$ radicals was observed. It can be inferred that the C–H bond cleavage of molecular HCHO is thermodynamically less favorable than the dehydrogenation of H_2O during the whole reaction of pristine MnO_2 . As for the U- MnO_2 sample (Fig. 7c), $\cdot OH$ radicals rapidly accumulated within 3 min, and the signals of DMPO-derived $\cdot H$, $\cdot OOH$, and $\cdot CO$ species were also observed, exhibiting relatively higher intensities than the corresponding signals for pristine MnO_2 . This shows that both the dehydrogenation of HCHO and the dissociation of water are thermodynamically favored on U- MnO_2 . In addition, the different types of free radicals formed during the reaction process in the aerobic neutral

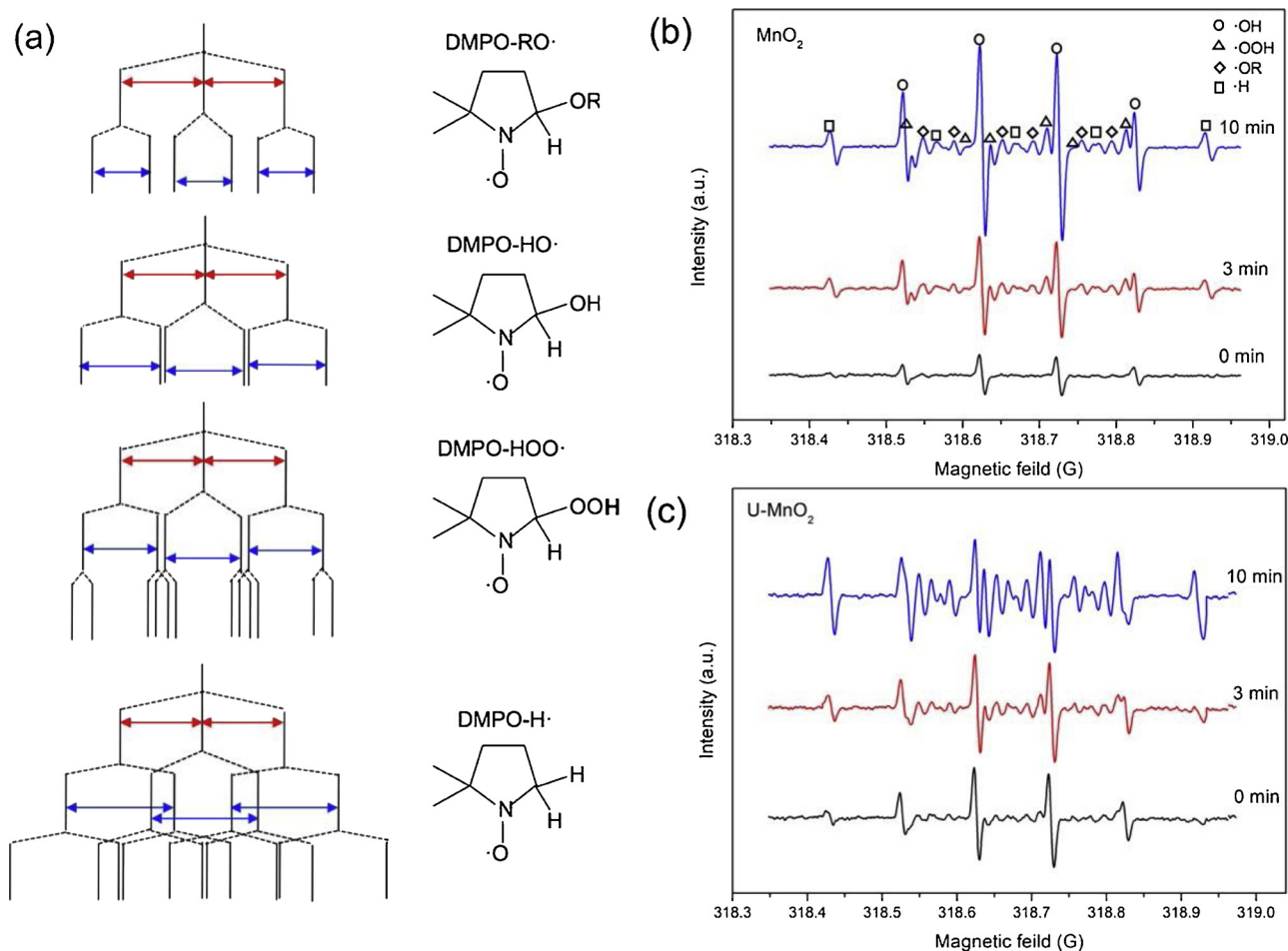


Fig. 7. (a) The structure of DMPO trapped radicals. (b) ESR DMPO adducts recorded in the systems containing HCHO, NaOH, H_2O , and MnO_2 or U- MnO_2 catalyst in open air from 0 to 10 min.

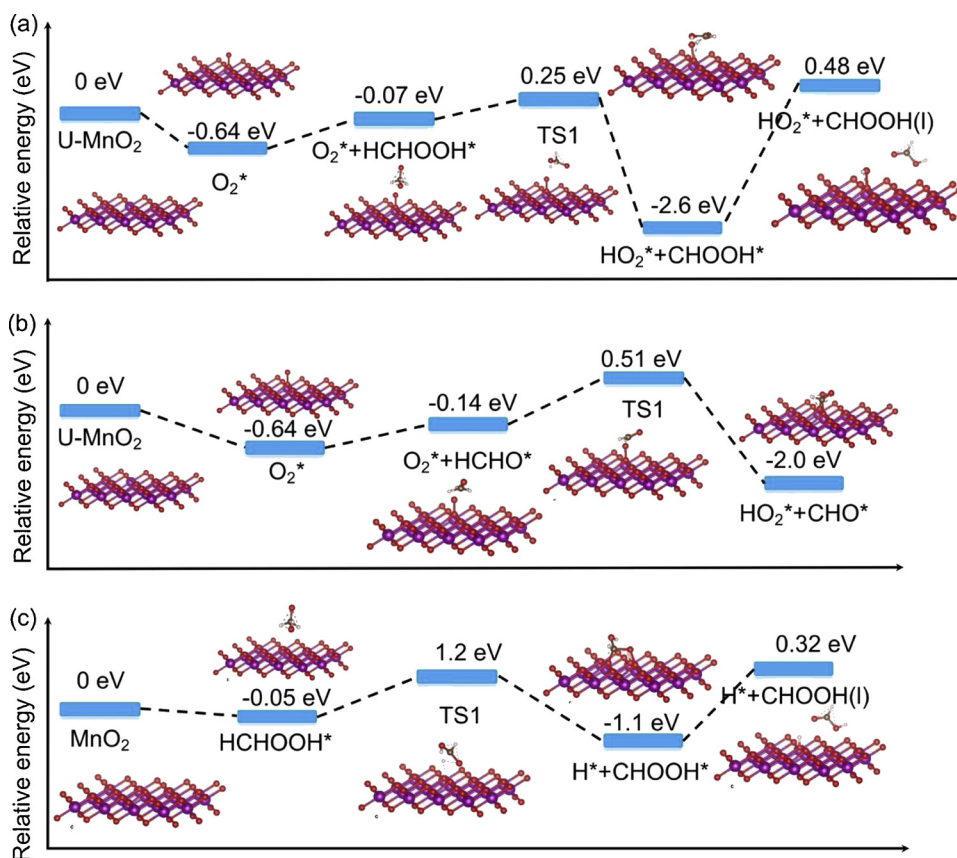


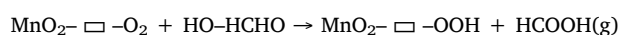
Fig. 8. Reaction path for dehydrogen process from formaldehyde: (a) Energy profiles for formaldehyde dissociation into H atom on U-MnO₂ in the systems containing HCHO, NaOH, and O₂. (b) Energy profiles for formaldehyde dissociation into H atom on U-MnO₂ in the systems only containing HCHO, and O₂. (c) Energy profiles for formaldehyde directly dissociation into H atom in the systems containing HCHO, and NaOH.

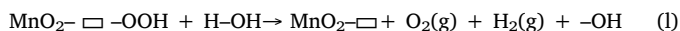
HCHO environment were also examined (Figure S10d). No signal of characteristic DMPO-trapped free radicals was observed, indicating alkaline environment present crucial conditions for H₂ evolution.

To better understand the hydrogen evolution reaction mechanism at the atomic level, we performed quantum chemical calculations based on density functional theory (DFT) calculations for reaction pathways for O–H bond cleavage of H₂O and C–H bond cleavage of HCHO on exposed (001) surfaces in pristine MnO₂ compared with those of U-MnO₂. One oxygen atom was removed from the perfect exposed (001) crystal facet to simulate U-MnO₂ structure, representing the presence of V_O on U-MnO₂. First, we compared the adsorption energies (*E*_{ads}) of molecular O₂, hydroxylated formaldehyde (HOHCHO), and H₂O adsorbed on V_O site (Figure S11). O₂ exhibited a significantly higher *E*_{ads} value (−0.64 eV) than that of H₂O (−0.37 eV) and HOHCHO (−0.46 eV), indicating O₂ molecular assuming end-on configuration preferred adsorption at V_O site by. Energy changes of the reaction pathways for the dihydrogen process on pristine MnO₂ and U-MnO₂ are illustrated in Fig. 8. As for U-MnO₂ reacted under basic condition (Fig. 8a), The dehydrogenation reaction consists of 5 configurations including 1 transition states (TS). The reaction started by O₂ adsorption on the oxygen vacancy sites. Then, alkaline HCHO in form of HO–HCHO, a kind of Cannizzaro tetrahedral intermediate, was transferred from the liquid phase to the solid surface and adsorbed at the O–O sites. The next step was the H abstraction from HO–HCHO by adsorbed ‘O₂– species, resulting in the generation of ‘OOH species. Then, HCOOH was desorbed from the (001) surface. The activation barriers (*E*_A) were found to be 0.32 eV for U-MnO₂. As for U-MnO₂ reacted under neutral condition (Fig. 8b), the reaction barrier with the formation of ‘OOH species directly from HCHO was calculated to be 0.5 eV, which was higher than that in the basic condition. The nucleophilic addition of a base to a carbonyl group enhanced the electron repelling ability of C=O, resulting in the weakening of the chemical bond between carbon and hydrogen atoms [48]. Thus, it could be

concluded that the dehydrogenation of HCHO is more favorable under alkaline conditions. As for pristine MnO₂ (Fig. 8c), *E*_{ads} of O₂ was calculated as −0.04 eV on MnO₂, which is much lower than that of U-MnO₂ (The saturated coordination structure with exposed (001) facet was not conducive to oxygen adsorption) (Figure S11). This result was further supported by a lower content of ‘O₂ radicals on pristine MnO₂ (the characteristic six peaks belongs to DMPO–‘O₂– [49–51]), as confirmed by the ESR spin-trapping experiment in a mixed catalyst sample and methanol suspensions (Figure S12). The react barrier of direct dehydrogenation from HOHCHO on MnO₂ was calculated to be 1.25 eV, which was higher than that of U-MnO₂ sample, suggesting that pristine MnO₂ was less reactive for C–H bond cleavage than U-MnO₂. The weak interactions between the pristine MnO₂ surface and molecular O₂ hindered the dehydrogenation process from HCHO.

The hydrogen evolution reaction between HCHO and H₂O actually involves two processes, one is the dehydrogenation of HCHO, and the other one is the dehydrogenation of H₂O, both of which may be the rate-limiting step of the entire reaction. Energy changes of the reaction pathways for the dihydrogen process from H₂O on U-MnO₂ are illustrated in Figure S13a. Considering that V_O are preferentially occupied by oxygen molecules, water molecules tend to adsorb on saturated coordinating oxygen atoms through weak interactions (second step in Figure S13a). Both of pristine MnO₂ and U-MnO₂ exhibited same react barrier with the value of 1.09 eV. Then, H atoms separately removed from water and formaldehyde combine to form H₂. Energy profiles for the generation of H₂ on U-MnO₂ (001) surface are illustrated in Figure S13b. This step consists of 6 configurations including 2 TS. H₂ and O₂ are generated from the interaction of ‘OOH–(Mn) and H–(O). This step is considered to be the whole rate-determining step (react barrier of 3.36 eV). At last, H₂, O₂, and OH were desorbed, completing the entire hydrogen evolution process. The entire reaction process can be illustrated as follows:





On the basis of above results and discussions, the whole mechanism was proposed. As for U-MnO₂, abundant surface oxygen vacancies occurred due to the disappearance of interlayer confinement along the c-axis direction. O₂ from gas phase could be adsorbed on V_O site by assuming the end-on configuration, forming 'O₂' radicals by one electron transfer process from 4f orbital of Mn³⁺ to π 2py* orbital of O₂. In addition, the presence of V_O also changed the surface electronic state, enhancing surface electron transfer property and promoting the activation of O₂ molecules. As a result, more content of surface adsorbed oxygen was detected on U-MnO₂ sample evidenced by XPS, O₂-TPD and EPR, further confirming V_O facilitated O₂ activation and dissociation process. As for the HCHO dehydrogenation experiment, U-MnO₂ exhibited higher activity than pristine MnO₂, and the hydrogen generation efficiency strongly related with partial pressure of the O₂, which further proved the important role of V_O. The formed 'O₂' species at V_O could easily attack one hydrogen from HCHO molecular with the generation of 'OOH radical. In the in-situ ESR experiment, more content of 'OOH radicals were observed on U-MnO₂, further confirming the function of V_O. Theoretical calculations of the reaction pathways demonstrated that direct dehydrogenation of alkaline HCHO was kinetically hindered owing to the high E_A value for the breaking of C–H bonds on pristine MnO₂, however, the energy barrier on the U-MnO₂ sample was suitable for both breaking O–H bonds and C–H bonds due to the presence of MnOO–HCHO transition state at V_O site, which accounted for the enhanced activity.

4. Conclusions

We have developed a method for ultra-thinning MnO₂ nanosheets by a strategy that consists of water swelling and subsequent CTAB-intercalation exfoliation. The thickness of the obtained ultrathin MnO₂ nanosheets is about 1–2 layers, exhibiting an enhanced H₂ evolution activity from alkaline HCHO solution. Ultrathin MnO₂ nanosheets facilitated O₂ activation and dissociation by its unique ultrathin structure and abundant V_O sites, triggering C–H bond cleavage at a lower energy from alkaline HCHO solution with the generation of more active 'OOH radicals. The decreased energy barrier facilitated the hydrogen evolution reaction from alkaline HCHO at room temperature. This work not only provides an applicable method for synthesizing ultrathin MnO₂ nanosheets but also gives an evidence toward understanding this hydrogen evolution reaction at the atomic level.

Acknowledgement

This project is supported by special fund of National Natural Science Foundation of China (21707107), State Key Joint Laboratory of Environment Simulation and Pollution Control (17K08ESPCT) and Suzhou-Tsinghua innovation guiding program (No. 2016SZ0104).

Appendix A. Supplementary data

Supplementary material related to this article can be found, in the online version, at doi:<https://doi.org/10.1016/j.apcatb.2019.02.047>.

References

- [1] X. Zou, Y. Zhang, Noble metal-free hydrogen evolution catalysts for water splitting, *Chem. Soc. Rev.* 44 (2015) 5148–5180, <https://doi.org/10.1039/C4CS00448E>.
- [2] L.E. Heim, H. Konnerth, M.H.G. Precht, Future perspectives for formaldehyde: pathways for reductive synthesis and energy storage, *Green Chem.* 19 (2017) 2347–2355, <https://doi.org/10.1039/c6gc03093a>.
- [3] J.W. Fu, J.G. Yu, C.J. Jiang, B. Cheng, g-C₃N₄-Based heterostructured photocatalysts, *Adv. Energy Mater.* 8 (2018) 1701503, <https://doi.org/10.1002/aenm.201701503>.
- [4] H. Yi, D.L. Huang, L. Qin, G.M. Zeng, C. Lai, M. Cheng, S.J. Ye, B. Song, X.Y. Ren, X.Y. Guo, Selective prepared carbon nanomaterials for advanced photocatalytic

- application in environmental pollutant treatment and hydrogen production, *Appl. Catal., B: Environ.* 239 (2018) 408–424, <https://doi.org/10.1016/j.apcatb.2018.07.068>.
- [5] H. Xu, J.J. Yi, X.J. She, Q. Liu, L. Song, S.M. Chen, Y.C. Yang, Y.H. Song, R. Vajtai, J. Lou, H.M. Li, S.Q. Yuan, J.J. Wu, P.M. Ajayan, 2D heterostructure comprised of metallic 1T-MoS₂/Monolayer g-C₃N₄ towards efficient photocatalytic hydrogen evolution, *Appl. Catal., B: Environ.* 220 (2018) 379–385, <https://doi.org/10.1016/j.apcatb.2017.08.035>.
- [6] H. Yi, D. Huang, L. Qin, G. Zeng, C. Lai, M. Cheng, S. Ye, B. Song, X. Ren, X. Guo, Selective prepared carbon nanomaterials for advanced photocatalytic application in environmental pollutant treatment and hydrogen production, *Appl. Catal. B: Environ.* 239 (2018) 408–424, <https://doi.org/10.1016/j.apcatb.2018.07.068>.
- [7] X.Y. Lu, J. Pan, E. Lovell, T.H. Tan, Y.H. Ng, R. Amal, A sea-change: manganese doped nickel/nickel oxide electrocatalysts for hydrogen generation from seawater, *Energy Environ. Sci.* 11 (2018) 1898–1910, <https://doi.org/10.1039/c8ee00976g>.
- [8] I. Roger, M.A. Shipman, M.D. Symes, Earth-abundant catalysts for electrochemical and photoelectrochemical water splitting, *Nat. Rev. Chem.* 1 (2017) 0003, <https://doi.org/10.1038/s41570-016-0003>.
- [9] S.Y. Jing, L.S. Zhang, L. Luo, J.J. Lu, S.B. Yin, P.K. Shen, P. Tsiakaras, N-doped porous molybdenum carbide nanobelts as efficient catalysts for hydrogen evolution reaction, *Appl. Catal., B: Environ.* 224 (2018) 533–540, <https://doi.org/10.1016/j.apcatb.2017.10.025>.
- [10] H. Lv, X. Chen, D.D. Xu, Y.C. Hu, H.Q. Zheng, S.L. Suib, B. Liu, Ultrathin PdPt bimetallic nanowires with enhanced electrocatalytic performance for hydrogen evolution reaction, *Appl. Catal., B: Environ.* 238 (2018) 525–532, <https://doi.org/10.1016/j.apcatb.2018.07.060>.
- [11] S. Emin, C. Altinkaya, A. Semerci, H. Okuyucu, A. Yildiz, P. Stefanov, Tungsten carbide electrocatalysts prepared from metallic tungsten nanoparticles for efficient hydrogen evolution, *Appl. Catal., B: Environ.* 236 (2018) 147–153, <https://doi.org/10.1016/j.apcatb.2018.05.026>.
- [12] R.D. Cortright, R.R. Davda, J.A. Dumesic, Hydrogen from catalytic reforming of biomass-derived hydrocarbons in liquid water, *Nature* 418 (2002) 964–967, <https://doi.org/10.1038/nature01009>.
- [13] L. Lin, W. Zhou, R. Gao, S. Yao, X. Zhang, W. Xu, S. Zheng, Z. Jiang, Q. Yu, Y. Li, C. Shi, X. Wen, D. Ma, Low-temperature hydrogen production from water and methanol using Pt/α-MoC catalysts, *Nature* 544 (2017) 80–83, <https://doi.org/10.1038/nature21672>.
- [14] L.E. Heim, N.E. Schlörer, J.H. Choi, M.H.G. Precht, Selective and mild hydrogen production using water and formaldehyde, *Nat. Commun.* 5 (2014) 3621, <https://doi.org/10.1038/ncomms4621>.
- [15] X.C. Sun, J. Lin, H.L. Guan, L. Li, L. Sun, Y.H. Wang, S. Miao, Y. Su, X.D. Wang, Complete oxidation of formaldehyde over TiO₂ supported subnanometer Rh catalyst at ambient temperature, *Appl. Catal., B: Environ.* 226 (2018) 575–584, <https://doi.org/10.1016/j.apcatb.2018.01.011>.
- [16] F. Liu, S.P. Rong, P.Y. Zhang, L.L. Gao, One-step synthesis of nanocarbon-decorated MnO₂ with superior activity for indoor formaldehyde removal at room temperature, *Appl. Catal., B: Environ.* 235 (2018) 158–167, <https://doi.org/10.1016/j.apcatb.2018.04.078>.
- [17] L. Qin, G. Zeng, C. Lai, D. Huang, P. Xu, C. Zhang, M. Cheng, X. Liu, S. Liu, B. Li, H. Yi, "Gold rush" in modern science: fabrication strategies and typical advanced applications of gold nanoparticles in sensing, *Coord. Chem. Rev.* 359 (2018) 1–31, <https://doi.org/10.1016/j.ccr.2018.01.006>.
- [18] H.Y. Hu, Z.B. Jiao, J.H. Ye, G.X. Lu, Y.P. Bi, Highly efficient hydrogen production from alkaline aldehyde solutions facilitated by palladium nanotubes, *Nano Energy* 8 (2014) 103–109, <https://doi.org/10.1016/j.nanoen.2014.05.015>.
- [19] S.P. Li, H.Y. Hu, Y.P. Bi, Ultra-thin TiO₂ nanosheets decorated with Pd quantum dots for high-efficiency hydrogen production from aldehyde solution, *J. Mater. Chem. A* 4 (2016) 796–800, <https://doi.org/10.1039/c5ta08720a>.
- [20] R.H. Li, X.H. Zhu, X.Q. Yan, H. Kobayashi, S. Yoshida, W.X. Chen, L.L. Du, K.C. Qian, B.L. Wu, S.H. Zou, L.F. Lu, W.Z. Yi, Y.H. Zhou, J. Fan, Oxygen-controlled hydrogen evolution reaction: molecular oxygen promotes hydrogen production from formaldehyde solution using Ag/MgO nanocatalyst, *ACS Catal.* 7 (2017) 1478–1484, <https://doi.org/10.1021/acscatal.6b03370>.
- [21] R.H. Li, X.H. Zhu, L.L. Du, K.C. Qian, B.L. Wu, S. Kawabata, H. Kobayashi, X.Q. Yan, W.X. Chen, All-solid-state magnesium oxide supported Group VIII and IB metal catalysts for selective catalytic reforming of aqueous aldehydes into hydrogen, *Int. J. Hydrogen Energy* 42 (2017) 10834–10843, <https://doi.org/10.1016/j.ijhydene.2017.02.041>.
- [22] L. Miao, J. Wang, P. Zhang, Review on manganese dioxide for catalytic oxidation of airborne formaldehyde, *Appl. Surf. Sci.* 466 (2019) 441–453, <https://doi.org/10.1016/j.apusc.2018.10.031>.
- [23] B. Liu, I.M. Mosa, W. Song, H. Zheng, C.H. Kuo, J.F. Rusling, S.L. Suib, J. He, Unconventional structural and morphological transitions of nanosheets, nanoflakes and nanorods of AuNP@MnO₂, *J. Mater. Chem. A* 4 (2016) 6447–6455, <https://doi.org/10.1039/C6TA02017H>.
- [24] J. Wang, P. Zhang, J. Li, C. Jiang, R. Yunus, J. Kim, Room-temperature oxidation of formaldehyde by layered manganese oxide: effect of water, *Environ. Sci. Technol.* 49 (2015) 12372–12379, <https://doi.org/10.1021/acs.est.5b02085>.
- [25] Y.Q. Guo, K. Xu, C.Z. Wu, J.Y. Zhao, Y. Xie, Surface chemical-modification for engineering the intrinsic physical properties of inorganic two-dimensional nanomaterials, *Chem. Soc. Rev.* 44 (2015) 637–646, <https://doi.org/10.1039/c4cs00302k>.
- [26] Y.W. Liu, C. Xiao, Z. Li, Y. Xie, Vacancy engineering for tuning electron and phonon structures of two-dimensional materials, *Adv. Energy Mater.* 6 (2016) 1600436, <https://doi.org/10.1002/aenm.201600436>.
- [27] Y.F. Sun, S. Gao, F.C. Lei, Y. Xie, Atomically-thin two-dimensional sheets for

- understanding active sites in catalysis, *Chem. Soc. Rev.* 44 (2015) 623–636, <https://doi.org/10.1039/c4cs00236a>.
- [28] H. Wang, S.C. Chen, D.Y. Yong, X.D. Zhang, S. Li, W. Shao, X.S. Sun, B.C. Pan, Y. Xie, Giant electron–hole interactions in confined layered structures for molecular oxygen activation, *J. Am. Chem. Soc.* 139 (2017) 4737–4742, <https://doi.org/10.1021/jacs.6b12273>.
- [29] C.H. Kuo, W. Li, L. Pahalagedara, A.M. El-Sawy, D. Kriz, N. Genz, C. Guild, T. Ressler, S.L. Suib, J. He, Understanding the role of gold nanoparticles in enhancing the catalytic activity of manganese oxides in water oxidation reactions, *Angew. Chem. Int. Ed.* 54 (2015) 2345–2350, <https://doi.org/10.1002/anie.201407783>.
- [30] J.Q. Yuan, Z.H. Liu, S.F. Qiao, X.R. Ma, N.C. Xu, Fabrication of MnO₂-pillared layered manganese oxide through an exfoliation/reassembling and oxidation process, *J. Power Sources* 189 (2009) 1278–1283, <https://doi.org/10.1016/j.jpowsour.2008.12.148>.
- [31] Y. Omomo, T. Sasaki, L.Z. Wang, M. Watanabe, Redoxable nanosheet crystallites of MnO₂ derived via delamination of a layered manganese oxide, *J. Am. Chem. Soc.* 125 (2003) 3568–3575, <https://doi.org/10.1021/ja021364p>.
- [32] W.J. Yang, Y.F. Zhu, F. You, L. Yan, Y.J. Ma, C.Y. Lu, P.Q. Gao, Q. Hao, W.L. Li, Insights into the surface–defect dependence of molecular oxygen activation over birnessite-type MnO₂, *Appl. Catal., B: Environ.* 233 (2018) 184–193, <https://doi.org/10.1016/j.apcatb.2018.03.107>.
- [33] H. Li, H. Shang, X.M. Cao, Z.P. Yang, Z.H. Ai, L.Z. Zhang, Oxygen vacancies mediated complete visible light NO oxidation via side-on bridging superoxide radicals, *Environ. Sci. Technol.* 52 (2018) 8659–8665, <https://doi.org/10.1021/acs.est.8b01849>.
- [34] J. Wang, J. Li, P. Zhang, G. Zhang, Understanding the “seesaw effect” of inter-layered K⁺ with different structure in manganese oxides for the enhanced formaldehyde oxidation, *Appl. Catal., B: Environ.* 224 (2018) 863–870, <https://doi.org/10.1016/j.apcatb.2017.11.019>.
- [35] S.L. Brock, N. Duan, Z.R. Tian, O. Giraldo, H. Zhou, S.L. Suib, A review of porous manganese oxide materials, *Chem. Mater.* 10 (1998) 2619–2628, <https://doi.org/10.1021/cm980227h>.
- [36] J.L. Wang, G.K. Zhang, P.Y. Zhang, Graphene-assisted photothermal effect promoting catalytic activity of layered MnO₂ for gaseous formaldehyde oxidation, *Appl. Catal., B: Environ.* 239 (2018) 77–85, <https://doi.org/10.1016/j.apcatb.2018.08.008>.
- [37] H. Wang, J.J. Zhang, X.D. Hang, X.D. Zhang, J.F. Xie, B.C. Pan, Y. Xie, Half-metallicity in single-layered manganese dioxide nanosheets by defect engineering, *Angew. Chem., Int. Ed.* 54 (2015) 1195–1199, <https://doi.org/10.1002/anie.201410031>.
- [38] C. Julien, M. Massot, R. Baddour-Hadjean, S. Franger, S. Bach, J.P. Pereira-Ramos, Raman spectra of birnessite manganese dioxides, *Solid State Ion.* 159 (2003) 345–356, [https://doi.org/10.1016/S0167-2738\(03\)00035-3](https://doi.org/10.1016/S0167-2738(03)00035-3).
- [39] W.S. Zhu, X. Gao, Q. Li, H.P. Li, Y.H. Chao, M.J. Li, S.M. Mahurin, H.M. Li, H.Y. Zhu, S. Dai, Controlled gas exfoliation of boron nitride into few-layered nanosheets, *Angew. Chem., Int. Ed.* 55 (2016) 10766–10770, <https://doi.org/10.1002/anie.201605515>.
- [40] Y.X. Chen, G.K. Tian, M.J. Zhou, Z.W. Huang, C.X. Lu, P.P. Hu, J.Y. Gao, Z.L. Zhang, X.F. Tang, Catalytic control of typical particulate matters and volatile organic compounds emissions from simulated biomass burning, *Environ. Sci. Technol.* 50 (2016) 5825–5831, <https://doi.org/10.1021/acs.est.5b06109>.
- [41] F. Xu, Z. Huang, P. Hu, Y. Chen, L. Zheng, J. Gao, X. Tang, The promotion effect of isolated potassium atoms with hybridized orbitals in catalytic oxidation, *Chem. Commun.* 51 (2015) 9888–9891, <https://doi.org/10.1039/c5cc02476e>.
- [42] S. Rong, P. Zhang, Y. Yang, L. Zhu, J. Wang, F. Liu, MnO₂ framework for instantaneous mineralization of carcinogenic airborne formaldehyde at room temperature, *ACS Catal.* 7 (2017) 1057–1067, <https://doi.org/10.1021/acscatal.6b02833>.
- [43] X.Y. Wang, Y. Liu, Y.Y. Zhang, T.H. Zhang, H.Z. Chang, Y.F. Zhang, L.L. Jiang, Structural requirements of manganese oxides for methane oxidation: XAS spectroscopy and transition-state studies, *Appl. Catal., B: Environ.* 229 (2018) 52–62, <https://doi.org/10.1016/j.apcatb.2018.02.007>.
- [44] J. Wang, J. Li, C. Jiang, P. Zhou, P. Zhang, J. Yu, The effect of manganese vacancy in birnessite-type MnO₂ on room-temperature oxidation of formaldehyde in air, *Appl. Catal., B: Environ.* 204 (2017) 147–155, <https://doi.org/10.1016/j.apcatb.2016.11.036>.
- [45] F.C. Lei, Y.F. Sun, K.T. Liu, S. Gao, L. Liang, B.C. Pan, Y. Xie, Oxygen vacancies confined in ultrathin indium oxide porous sheets for promoted visible-light water splitting, *J. Am. Chem. Soc.* 136 (2014) 6826–6829, <https://doi.org/10.1021/ja501866r>.
- [46] Y.X. Zhao, C. Chang, F. Teng, Y.F. Zhao, G.B. Chen, R. Shi, G.I.N. Waterhouse, W.F. Huang, T.R. Zhang, Defect-engineered ultrathin δ-MnO₂ nanosheet arrays as bifunctional electrodes for efficient overall water splitting, *Adv. Energy Mater.* 7 (2017) 1700005, <https://doi.org/10.1002/aenm.201700005>.
- [47] Y.F. Sun, Q.H. Liu, S. Gao, H. Cheng, F.C. Lei, Z.H. Sun, Y. Jiang, H.B. Su, S.Q. Wei, Y. Xie, Pits confined in ultrathin cerium(IV) oxide for studying catalytic centers in carbon monoxide oxidation, *Nat. Commun.* 4 (2013) 2899, <https://doi.org/10.1038/ncomms3899>.
- [48] E.C. Ashby, F. Doctorovich, C.L. Liotta, H.M. Neumann, E.K. Barefield, A. Konda, K. Zhang, J. Hurley, D.D. Siemer, Concerning the formation of hydrogen in nuclear waste. Quantitative generation of hydrogen via a Cannizzaro intermediate, *J. Am. Chem. Soc.* 115 (1993) 1171–1173, <https://doi.org/10.1021/ja00056a065>.
- [49] N. Zou, Q. Nie, X.R. Zhang, G.K. Zhang, J.L. Wang, P.Y. Zhang, Electrothermal regeneration by Joule heat effect on carbon cloth based MnO₂ catalyst for long-term formaldehyde removal, *Chem. Eng. J.* 357 (2019) 1–10, <https://doi.org/10.1016/j.cej.2018.09.117>.
- [50] B. Li, C. Lai, G. Zeng, L. Qin, H. Yi, D. Huang, C. Zhou, X. Liu, M. Cheng, P. Xu, C. Zhang, F. Huang, S. Liu, Facile hydrothermal synthesis of Z-scheme Bi₂Fe₄O₉/Bi₂WO₆ heterojunction photocatalyst with enhanced visible light photocatalytic activity, *ACS Appl. Mater. Interfaces* 10 (2018) 18824–18836, <https://doi.org/10.1021/acsami.8b06128>.
- [51] C. Lai, M. Zhang, B. Li, D. Huang, G. Zeng, L. Qin, X. Liu, H. Yi, M. Cheng, L. Li, Z. Chen, L. Chen, Fabrication of CuS/BiVO₄ (0 4 0) binary heterojunction photocatalysts with enhanced photocatalytic activity for Ciprofloxacin degradation and mechanism insight, *Chem. Eng. J.* 358 (2019) 891–902, <https://doi.org/10.1016/j.cej.2018.10.072>.